Grain-Displacive Gas Migration in Fine-grained Sediments

Zhonghao Sun[1] and J. Carlos Santamarina[1]

Abstract: Gas migration mechanisms control the release of gas from seafloor sediments. We study underlying phenomena using transparent sediments subjected to controlled effective stress; this experimental approach allows high-resolution real-time monitoring of gas migration through cohesionless granular materials under 3D-boundary conditions. Observed migration patterns depend on the effective stress at the time of injection and the stress history. Gas migration transitions from pore-invasive to grain-displacive when the capillary pressure for air entry ΔP_{AE} is greater than the effective stress σ'. This study focuses on grain-displacive gas migration. The morphology of grain-displacive gas bodies changes with depth as the sediment stiffness G increases and the effect of surface tension γ vanishes: spheroidal gas bubbles form in the near-surface, faceted cavities further down, and eventually open-mode fractures develop at depth. The gas injection pressure is proportional to the effective stress in grain-displacive migration. Pre-loading and overconsolidation cause the rotation of principal stresses and gas-driven openings align with the new minimum principal stress direction. Cyclic loading promotes the upwards migration of gas-filled openings, and there is mechanical memory of previous gas pathways in sediments.

Keywords: methane leakage, gas migration, soft sediments, hydraulic fracturing, seafloor

Corresponding author: Zhonghao Sun (zhonghao.sun@kaust.edu.sa)

Affiliation: [1]Earth Science and Engineering, King Abdullah University of Science and Technology (KAUST), Thuwal 23955-6900, Saudi Arabia.

Introduction

There is widespread methane release from submerged and surface sediments into the atmosphere. Persistent methane bubble curtains rise above various seafloor locations worldwide, including the West Spitsbergen continental margin [Westbrook et al., 2009], the northern US Atlantic margin [Skarke et al., 2014], the sea of Marmara [Tary et al., 2012], the Gulf of Mexico [Wang et al., 2016], and the Håkon Mosby Mud Volcano [Sauter et al., 2006]. Similarly, methane is released from sediments in lakes and swamps [Scandella et al., 2011]. The released methane is biogenic when it originates from shallow organic matter accumulations, or thermogenic when produced at depth.

Gas migration mechanisms in soft sediments control gas release events [Dupre et al., 2015; Scandella et al., 2017], determine the formation of craters and pockmarks [Riboulot et al., 2016; Andreassen et al., 2017; de Prunele et al., 2017], and constrain the potential gas recovery strategies from methane hydrate accumulations in shallow marine sediments [Moridis et al., 2011; Fauria and Rempel, 2011; Jang, 2014]. Gas migration pathways are also relevant to other degassing processes such as subsurface CO_2 leakage [Lewicki et al., 2007; Bang et al., 2013; Cevatoglu et al., 2015] and gas-driven volcanic eruptions [Suckale et al., 2016].

We can anticipate two end-members for gas transport in sediments as a function of the air entry pressure ΔP_{AE} relative to the effective stress σ' [Clayton and Hay, 1994; Clennell et al., 2000; Shin and Santamarina, 2010; Dai et al., 2012; Holtzman et al., 2012]: either gas invades from pore-to-pore and creates viscous and capillary fingers (expected in coarse-grained sediments at depth), or gas displaces the sediment grains and creates preferential

pathways (expected in shallow, fine-grained sediments). This study focuses on grain-displacive gas migration in sediments.

A limited number of studies have directly observed grain-displacive gas migration processes in sediments. While theoretical solutions often assume spherical gas inclusions in shallow sediments [Wheeler, 1988, 1990; Sills and Wheeler, 1992; Pietruszczak and Pande, 1996], experimental studies have shown other forms such as oblate spheroids, fingers, and fractures [Johnson et al., 2002; Sandnes et al., 2011]. Most of these experiments used thin quasi-2D Hele-Shaw cells [Chevalier et al., 2009; Sandnes et al., 2011; Huang et al., 2012; Saintyves et al., 2013; Oppenheimer et al., 2015; Varas et al., 2015; Eriksen et al., 2015; Campbell et al., 2017]. Some tests involved transparent gels [Johnson et al., 2002; Boudreau et al., 2005]. Others observed gas inclusions using X-ray CT scans [Abegg and Anderson, 1997; Anderson et al., 1998; Barry et al., 2010]. These approaches have limitations related to CT scan time relative to process time, frictional boundaries and altered state of stress in Hele-Shaw cells, fundamental material differences between the elastic and cohesive gels versus the inherently granular nature of sediments, i.e., effective stress-dependent frictional strength τ, stiffness G, and dilatancy ψ [Santamarina et al., 2001].

The purpose of this study is to investigate gas migration mechanisms in soft fine-grained sediments under 3D field conditions. Open-mode discontinuities in cohesionless granular media are inherently grain-displacive and fundamentally different from tensile fractures in elastic cohesive materials where linear elastic fracture mechanics applies [Shin and Santamarina, 2011b]. Therefore we use a transparent granular material and subject the medium to various effective stress levels to simulate gas migration in sediment columns at different depths. While we emphasize the cohesionless nature of the sediments (i.e., frictional), we use the term "fracture" to describe open-mode discontinuities for simplicity.

Materials and Methods

Transparent Soil

Transparent soils consist of solid clear grains mixed with a liquid of the same refractive index [Iskander, 2010]. Due to their high transparency and granular nature, transparent soils support the study of complex engineering problems such as multiphase flow, pile penetration, failure of shallow foundations, and tunneling [Gill and Lehane, 2001; Iskander, 2010; Liu and Iskander, 2010]. Transparent porous media coupled with planar laser-induced fluorescence and digital image correlation can provide 3D information on fluid invasion topology [Krummel et al., 2013; Dalbe and Juanes, 2018].

The transparent soil used in this study consists of fumed silica mixed with an oil blend (similar to Gill and Lehane, 2001). Fine fumed silica particles (diameter~30nm, density=2.2 g/cm^3, from Sigma-Aldrich) form porous micron-size aggregates. The oil blend that matches the refractive index of fumed silica is a 1:1 mixture of two commercially available baby oils (from Mom to Mom and Johnson's®). The oil blend has a viscosity of 20 mPa·s and its density is 0.825 g/mL. The preparation procedure involves three steps: (1) mix 3g of fumed silica for every 40mL of blended oil to form a mobile slurry; (2) vacuum the slurry for a few hours to remove all air bubbles so that the slurry becomes transparent; (3) consolidate the slurry to the desired effective stress.

Table 1 summarizes the geotechnical properties of the transparent soil. The nano-size grains define its high specific surface S_s=200m^2/g. However, the micron-size inter-aggregate pores determine its air entry pressure ΔP_{AE}≈200kPa. The measured shear wave velocity vs. stress parameters (α, β, see supporting information Text S1 for details), consolidation parameters (C_c, $e_{1\text{kPa}}$, c_v), friction angle ϕ, and the liquid limit *LL* confirm that this transparent

granular medium is a true analogue for fine-grained clayey sediments.

Experimental Devices and Procedure

The transparent test cell has a square cross-section to facilitate recording the gas migration processes without geometric distortion (Plexiglas cell of square cross-section, width a=50.8 mm, wall thickness 3.2 mm). The test cell and reaction frame allow for vertical loading, time-dependent consolidation, fluid drainage, and gas injection (**Figure 1-a**). A pneumatic cylinder pushes a permeable porous disk to apply the vertical load while a linear variable displacement transducer (LVDT, Trans-Tek Inc.) monitors the vertical displacement. The excess pore fluid can drain from both the top and bottom plates; double drainage shortens the drainage path to half the specimen height, and consolidation becomes 4 times faster than for single drainage. The stainless steel needle used for gas injection (cylindrical tube, ID=0.83 mm, OD=1.27 mm) is fixed at the center of the bottom plate and connects to a pressure transducer (Omega PX209) and a syringe pump (Braintree Scientific Inc, BS-8000). There are two cameras (Sony α5000) mounted normal to each other and two LED panels provide background illumination. The two orthogonal views allow the 3D characterization of the gas migration process.

We pour the transparent slurry into the cell and consolidate it to the desired effective stress level. A metal wire inserted inside the needle prevents particle entry and clogging during the consolidation process. After consolidation, we remove the metal wire and connect the needle to the syringe pump (**Figure 1-b**). The syringe pump injects gas at a low constant rate (2 mL/hr). We record the pressure signature and gather still images 6 times per minute.

Boundary Effects

Cell dimensions minimize boundary effects while maintaining high-quality see-

through conditions. The cell width a=50.8 mm is limited by transparency; for this width, we anticipate negligible transverse boundary effects for gas bubbles that are smaller than 10 mm [Yu, 2013]. On the other hand, we keep a good distance between the injection point and the top boundary to observe gas migration; wall friction accumulates with depth and causes a lower vertical effective stress at the injection point compared to the stress applied at the top surface (Janssen effect - Sperl, 2006). We selected the specimen height-to-width ratio as a compromise between these competing effects. The expected decrease in vertical effective stress is ~20% at a sediment depth z=0.5a and ~34% at z=a if wall friction is fully mobilized [Briscoe and Rough, 1998]. The supporting information Text S2 associated to this paper provides a detailed discussion on wall friction.

Results

Gas Migration Patterns and Pressure Signatures

We consolidate transparent soil specimens to vertical effective stress levels between σ'_v=0.15 kPa and σ'_v=44 kPa (at the top surface, z=0). These conditions correspond to effective stresses in shallow marine sediment columns that range from less than 10 cm to more than 10 m high estimated using published sediment density data [Hamilton, 1976]. The core of the study comprises 21 separate experiments. **Figure 2** shows typical results at σ'_v=0.15 kPa, 3.8 kPa, and 24 kPa.

Gas migrates as bubbles at σ'_v=0.15 kPa. Bubbles are non-spherical, and sequential bubbles interact and may merge as they migrate upwards. The pressure signature shows pressurization until the gas bubble starts forming; the sudden pressure drop during bubble inflation ends as the bubble is released (See other examples in Fainerman et al., 2004).

Sequential formation-release events lead to the recorded saw-tooth pressure signal in **Figure 2-I**.

At an intermediate consolidation stress of σ'_v=3.8 kPa, the growing gas inclusion starts as a 3D cavity and transitions into a thin fracture later on. The initial cavity deviates from the smooth spheroidal bubbles in slurries and exhibits a faceted geometry; this indicates that the role of the surface tension vanishes as a shape-controlling parameter (**Figure 2-II-a**). The gas cavity grows as a succession of expansion events. The gas pressure drops suddenly when the cavity forms and enlarges. Gradually, the cavity develops corners and edges (**Figure 2-II-b**); local fractures initiate at these sharp locations and eventually grow to form a single thin fracture (**Figure 2-II-c**).

At higher effective stress levels (e.g. σ'_v=24 kPa, **Figure 2-III**), gas invades the transparent soil by creating fractures from the onset, and there is no early cavity expansion stage. The injection pressure reaches a plateau that is characterized by small pressurization-drop cycles, i.e., saw-tooth shape as well. Each pressure drop signifies a step growth in the fracture volume.

The fracture plane becomes thinner as the effective stress increases (e.g., σ'_v=44 kPa, **Figure 3**). The gas pressure increases continuously during fracture growth. The pressure buildup causes fast fracture development. This trend suggests that the injected gas volume is larger than the created fracture opening volume.

Boyle's law for ideal gas allows us to calculate the volume of the gas inclusion V_{gi} as it develops in the transparent soil specimen:

$$P \cdot \left(V_{sys} - V_{inj} + V_{gi} \right) = C \qquad (1)$$

where P is the gas pressure, V_{sys} is the initial volume of gas in the injection system, and V_{inj} is

the injected gas volume. We estimate the constant C from P-V_{inj} values before a gas inclusion forms. Figure 2 shows the computed gas inclusion volumes for cases II and III. The sudden volume jumps are consistent with concurrent visual observations.

Stress History

Two additional experiments explore gas injection into "overconsolidated" specimens, i.e., specimens preloaded to high vertical effective stress σ'_{vm} and then unloaded to a lower stress level σ'_v. The goal is to cause principal stress rotation so that the vertical stress becomes the minimum principal stress σ'_3: $\sigma'_3=\sigma'_v$. The overconsolidation ratio $OCR=\sigma'_{vm}/\sigma'_v$ and the vertical effective stress at injection σ'_v define experimental conditions. The residual horizontal effective stress after unloading can be estimated as $\sigma'_h=(1-\sin\phi)OCR^{\sin\phi}\cdot\sigma'_v$ [Mayne and Kulhawy, 1982]. The friction angle of the transparent soil is ϕ=30°, then $\sin\phi$=0.5 and principal stress rotation $\sigma'_h > \sigma'_v$ is anticipated when OCR>4.

We run a test using a short overconsolidated specimen with an estimated OCR=10 at the injection point. The sediment experiences principal stress rotation at the injection point, and gas invasion nucleates a horizontally oriented thin fracture. The fracture propagates horizontally and eventually tilts as it feels the cell walls (Figure S2 in supporting information).

The test run with a tall specimen has an estimated overconsolidation ratio OCR=1.5 at the injection point and OCR>10 close to the top plate. As a result, the fracture initiates and propagates vertically and tilts at mid height when it "feels" the principal stress rotation, i.e., the horizontal effective stress becomes larger than the vertical effective stress (**Figure 3**).

Degassing and Fracture Healing

Gas releases into the water column or the atmosphere once it reaches the sediment

surface. Gas release events are intermittent or continuous depending on (1) the gas injection rate which determines the gas re-pressurization time, and (2) the sediment properties and stress conditions that determine the fracture healing time. There is a sudden drop in gas pressure when the pressurized gas in fractures leaks out; then, the gas pressure starts to build up again until another degassing event occurs. Sediments "heal" and the fracture gradually closes after each gas release event. Healing diminishes with successive degassing events; eventually, the degassing pathway may remain open and gas would leak continuously at a relatively constant pressure (**Figure 3**). Experiments at low effective stresses exhibit wide openings that require long healing times, thus gas continues degassing and there is low gas pressure buildup (short re-pressurization time).

Cyclic Loading (Unloading and Reloading)

Several tests include vertical stress cycles after gas injection to examine the effects of cyclic loading on gas migration. These tests resemble fluid pressure oscillations associated with tides (see wave-seabed interactions in Jeng, 2003). **Figure 4** shows an example of a specimen with an initial Y-shaped gas fracture after gas injection stopped. The gas expands during vertical unloading from 14 kPa to 0, the fracture advances upwards, reaches the top porous disk, and leaks gas into the atmosphere. During vertical reloading, the gas inclusion partially closes and the leak pathway temporarily shuts off. Eventually, it reopens again during the following unloading cycle. Other similar cases tested as part of this study show the gradual upwards migration of gas inclusions during cyclic loading (see similar observations in Wheeler, 1990).

Memory Effect

Gas migration follows similar pathways during successive injections; this suggests

that there is mechanical memory of previous events in sediments. Images in **Figure 2-I** show that individual bubbles move along the same trajectory created by the leading bubble at low effective stress. Similarly, there is memory in the fracture formation regime, as demonstrated in **Figure 5**: the gas-filled fracture (σ'_v=4 kPa) gradually closes as gas diffuses into the medium during the following 4 days. The second gas injection at the same vertical effective stress follows a migration pattern very similar to the opening created during the first injection. The similarities are not only in overall geometry, but also in the fine details; for example, both have the same broken-curved geometry next to the needle (front view), and vein patterns (side view). Memory remains in the sediment even when successive gas injections are separated by long inactive periods.

Mechanical memory reflects grain-scale displacements during the first injection: the subsequent relaxation during deflation causes local changes in horizontal effective stress (lower σ') and local void ratio (higher e). Similar mechanisms for sediment memory were observed in contracting cavities in soils [Yu and Rowe, 1999; Cheng et al., 2007] and in the evolution of horizontal effective stress and void ratio during mineral dissolution [Shin et al., 2008; Cha and Santamarina, 2014]. Local sediment fabric changes and entrapped gas micro-pockets may contribute to the memory effect.

Analysis and Discussion

Gas Migration Patterns in Fine-grained Sediments

Transparent soil specimens allow us to observe gas migration in granular media in real time and with high resolution. Our results reveal that gas migration patterns in fine-grained sediments depend on the effective stress at the time of injection and the stress history,

as they determine all the sediment mechanical properties, in particular its stiffness. **Figure 6** summarizes the evolving morphology of gas inclusions as a function of vertical effective stress σ'_v and sediment shear stiffness G (Note: shear stiffness is calculated from the measured shear wave velocity V_S and sediment density ρ: $G=\rho V_s^2$). We used image analysis to measure the inclusion area S from the two orthogonal directions (theorem for orthogonal projections of a plane), and the injection P-V data to compute the gas inclusion volume V_{gi} (equation 1). Then, the average thickness of the gas inclusion is $th=V_{gi}/S$.

Results in **Figure 6** show that gas inclusions flatten and the thickness-to-width ratio th/W decreases as the sediment stiffness G increases with effective stress. Results from this study on grain-displacive gas migration and previously published results on gas invasion [Shin and Santamarina, 2010; Sandnes et al., 2011; Holtzman et al., 2012; Dai et al., 2012] allow us to conclude that gas migration patterns evolve from grain-displacive at low effective stress and stiffness (bubbles, tubes, faceted cavities, and open-mode fractures) to pore-invasive when the sediment is stiff at high effective stress:

- The dimensionless ratio $\Pi_{bubble}=GR/\gamma$ captures the balance between sediment stiffness G and surface tension γ as morphology-control parameters, where R is the bubble radius. The change in gas inclusion geometry from a smooth-spheroidal at low Π_{bubble} to a faceted cavity marks the transition from surface tension γ-controlled to sediment stiffness G-controlled bubble growth.
- Analyses and results show preferential planar openings or "fractures" rather than cavity expansion when Π_{bubble} increases and the sediment becomes stiffer. The measured thickness-to-width ratio th/W are inversely related to the sediment stiffness G, $(th/W) \propto G^{-1}$, as anticipated from theory of elasticity.
- The sediment stiffness at high effective stress prevents grain displacement and the

gas-liquid interface invades pores. The transition from grain-displacement to pore-invasion is captured in the dimensionless ratio between grain-scale capillary forces and effective stress-dependent skeletal forces: $\Pi_{inv}=10\gamma/(\sigma' d_{grain})$ where d_{grain} is the particle size. In terms of the air entry pressure ΔP_{AE}, this dimensionless ratio is $\Pi_{inv}=\Delta P_{AE}/\sigma'$ (see Shin and Santamarina, 2011b). Pore-invasion takes place at $\sigma' \approx 200$ kPa in the tested transparent soil.

Our results contrast with observations in quasi-2D Hele-Shaw cells and with transparent gels. Experiments in Hele-Shaw cells cannot control effective stress and the frequently observed fractal patterns are determined by side friction under the quasi-2D boundary conditions [Sandnes et al., 2011; Oppenheimer et al., 2015; Varas et al., 2015; Campbell et al., 2017]. On the other hand, effective stress-dependent gas migration patterns are not observed in experiments with transparent gelatins because of their cohesive nature [Johnson et al., 2002; Boudreau et al., 2005].

Fracture Growth Process

At the grain scale, the air-liquid interface invades the sediment at large pores or defects and pushes grains aside (**Figure 7a**). Grain-displacive gas migration increases the sediment pore size, and decreases contact forces between grains ahead of the fracture tip [Santamarina, 2003; Shin and Santamarina, 2011a&b; Zhang et al. 2013]. These grain-scale mechanisms create the positive feedback that sustains further fracture growth.

The interface between the invading gas body and the transparent soil is faceted and irregular: in agreement with visual observations, open-mode discontinuities do not grow as a single front but rather by successive opening events (grain-displacive, see **Figure 7b** for front view, and **Figure 7c, d** for side view). The front advances along the plane perpendicular to

the minimum effective stress, as it is clearly demonstrated in tests with overconsolidated sediments where the fracture tilts in response to the principal stress rotation (**Figure 3**).

Gas Injection Pressure

The critical injection pressure at fracture opening affects the analysis of multiple engineering tasks such as drilling [Keulen, 2001], hydraulic conductivity measurements [Bjerrum et al., 1972], in situ remediation for low-permeability soils [Alfaro and Wong, 2001], and grouting [Marchi et al., 2013]. Most analytical solutions consider tensile strength and assume linear elastic fracture mechanics, in contrast to the cohesionless, granular nature of soft sediments. Instead, we adopt a frictional Mohr-Coulomb critical state formulation [Schofield and Wroth, 1968; Wood, 1990]. Injection pressures for cavity expansion and fracture propagation follow.

The internal pressure for a spherical cavity expansion P_{cavity} must work against the mean effective stress σ'_o, the pore fluid pressure u_o, and the soil resistance [Carter et al., 1986; Cao et al., 2001; Yu, 2013]:

$$P_{cavity} = \frac{4s_u}{3}\left[1+\ln\left(\frac{G}{s_u}\right)\right] + \sigma'_o + u_o \qquad (2)$$

where G is the shear stiffness of the soil, and s_u is the undrained shear strength [Cao et al., 2001; Mayne, 2001]:

$$s_u = \frac{1}{2}\sigma'_v \sin\phi\left(OCR\right)^{\Lambda} \qquad (3)$$

The exponent is Λ=0.8 to 0.9. Note that this model disregards surface tension around bubbles.

On the other hand, an open-mode gas-driven fracture propagates perpendicular to the minimum principal stress direction, and the injection pressure $P_{fracture}$ tends to the minimum

principal stress σ'_3 as the fracture size increases:

$$P_{fracture} = \sigma'_3 + u_o \quad (4)$$

Figure 8 compares the gas injection pressures for cavity expansion and fracture propagation as a function of the vertical effective stress at the injection point. Circles indicate observed cavity expansions and squares correspond to observed fractures. Experimental observations support model predictions. Overall, open-mode fracture propagation prevails, except at low effective stresses where gas invades as cavity-type bubbles in the low Π_{bubble} regime.

Conclusions

We visualized gas migration patterns in fine-grained sediments using transparent soil specimens subjected to various effective stress levels in 3D vessels. The transparent soil is a proper analogue of fine-grained sediments: it is granular, porous, frictional, and has effective stress-dependent stiffness and strength. Image analysis and gas injection pressure measurements provide quantitative information for mechanistic analyses. The main conclusions follow:

- Gas migration patterns reflect a competition between grain-scale capillary forces and effective stress-dependent skeletal forces. Gas migration is grain-displacive at low effective stress and high air entry pressure so that $\Pi_{inv}=\Delta P_{AE}/\sigma' \gg 1$, and becomes pore-invasive when $\Pi_{inv}=\Delta P_{AE}/\sigma' \ll 1$.
- In the grain-displacive regime, the morphology of the invading gas body varies with the effective stress: it starts with spheroidal gas bubbles at very shallow depth (low Π_{bubble}), evolves into faceted cavities, and eventually becomes open-mode fractures as the

effective stress increases with depth (high Π_{bubble}). The fracture plane thickness is inversely proportional to the sediment shear stiffness.

- Open-mode fractures grow perpendicular to the minimum principal effective stress σ'_3. Therefore, fractures are vertical in normal consolidated sediments and rotate with the principal effective stresses in overconsolidated sediments. The gas injection pressure is proportional to σ'_3.
- The gas body can migrate upwards along the sediment column. Besides the buoyancy drive, pressure fluctuations promote upwards migration of gas-filled openings.
- Displacive gas pathways may close during inactive injection periods. However, they can re-open with a similar morphology and at a lower pressure when gas injection continues. The mechanical memory of displacive pathways in sediments is associated to local changes in effective stress and void ratio. Memory remains even when gas flow ceases for prolonged periods.

Acknowledgments

Support for this research was provided by the KAUST endowment. G. E. Abelskamp edited the manuscript. Data sets presented as part of this study are available from the KAUST Repository: http://hdl.handle.net/10754/630965.

Reference

1. Abegg, F., & Anderson, A. L. (1997). The acoustic turbid layer in muddy sediments of Eckernfoerde Bay, Western Baltic: methane concentration, saturation and bubble characteristics. *Marine Geology*, *137*(1), 137-147.
2. Alfaro, M. C., & Wong, R. C. (2001). Laboratory studies on fracturing of low-permeability soils. *Canadian Geotechnical Journal*, *38*(2), 303-315.
3. Anderson, A. L., Abegg, F., Hawkins, J. A., Duncan, M. E., & Lyons, A. P. (1998). Bubble populations and acoustic interaction with the gassy floor of Eckernförde Bay. *Continental Shelf Research*, *18*(14), 1807-1838.
4. Andreassen, K., Hubbard, A., Winsborrow, M., Patton, H., Vadakkepuliyambatta, S., Plaza-Faverola, A., Gudlaugsson, E., Serov, P., Deryabin, A., Mattingsdal, R., Mienert, J., & Bunz, S. (2017). Massive blow-out craters formed by hydrate-controlled methane expulsion from the Arctic seafloor. *Science*, *356*(6341), 948-953.
5. Bang, E. S., Son, J. S., & Santamarina, J. C. (2013). Subsurface CO2 leakage: Lab-scale study of salient characteristics and assessment of borehole-based detection using resistivity tomography. In *Geotechnical and Geophysical Site Characterization 4*. Taylor & Francis Group London.
6. Barry, M. A., Boudreau, B. P., Johnson, B. D., & Reed, A. H. (2010). First-order description of the mechanical fracture behavior of fine-grained surficial marine sediments during gas bubble growth. *Journal of Geophysical Research: Earth Surface*, *115*(F4).
7. Bjerrum, L., Nash, J. K. T. L., Kennard, R. M., & Gibson, R. E. (1972). Hydraulic fracturing in field permeability testing. *Geotechnique*, *22*(2), 319-332.
8. Boudreau, B. P., Algar, C., Johnson, B. D., Croudace, I., Reed, A., Furukawa, Y., ... & Gardiner, B. S. (2005). Bubble growth and rise in soft sediments. *Geology*, *33*(6), 517-520.
9. Briscoe, B. J., & Rough, S. L. (1998). The effects of wall friction in powder compaction. *Colloids and Surfaces A: Physicochemical and Engineering Aspects*, *137*(1-3), 103-116.
10. Campbell, J. M., Ozturk, D., & Sandnes, B. (2017). Gas-Driven Fracturing of Saturated Granular Media. *Physical Review Applied*, *8*(6), 064029.
11. Cao, L. F., Teh, C. I., & Chang, M. F. (2001). Undrained cavity expansion in modified Cam clay. *Geotechnique*, *51*(4), 323-34.
12. Carter, J. P., Booker, J. Y., & Yeung, S. K. (1986). Cavity expansion in cohesive frictional

soils. *Geotechnique*, *36*(3), 349-358.

13. Cevatoglu, M., Bull, J. M., Vardy, M. E., Gernon, T. M., Wright, I. C., & Long, D. (2015). Gas migration pathways, controlling mechanisms and changes in sediment acoustic properties observed in a controlled sub-seabed CO2 release experiment. *International Journal of Greenhouse Gas Control*, *38*, 26-43.
14. Cha, M., & Santamarina, J. C. (2014). Dissolution of randomly distributed soluble grains: post-dissolution k 0-loading and shear. *Geotechnique*, *64*(10), 828-836.
15. Cha, M., Santamarina, J. C., Kim, H. S., & Cho, G. C. (2014). Small-strain stiffness, shear-wave velocity, and soil compressibility. *Journal of Geotechnical and Geoenvironmental Engineering*, *140*(10), 06014011.
16. Cheng, C. Y., Dasari, G. R., Chow, Y. K., & Leung, C. F. (2007). Finite element analysis of tunnel–soil–pile interaction using displacement controlled model. *Tunnelling and Underground Space Technology*, *22*(4), 450-466.
17. Chevalier, C., Lindner, A., Leroux, M., & Clément, E. (2009). Morphodynamics during air injection into a confined granular suspension. *Journal of Non-newtonian Fluid Mechanics*, *158*(1-3), 63-72.
18. Clayton, C. J., & Hay, S. J. (1994). Gas migration mechanisms from accumulation to surface. *Bulletin of the Geological Society of Denmark*, *41*(1), 12-23.
19. Clennell, M. B., Judd, A., & Hovland, M. (2000). Movement and accumulation of methane in marine sediments: relation to gas hydrate systems. In *Natural Gas Hydrate* (pp. 105-122). Springer Netherlands.
20. Dai, S., Santamarina, J. C., Waite, W. F., & Kneafsey, T. J. (2012). Hydrate morphology: Physical properties of sands with patchy hydrate saturation. *Journal of Geophysical Research: Solid Earth*, *117*(B11).
21. Dalbe, M. J., & Juanes, R. (2018). Morphodynamics of Fluid-Fluid Displacement in Three-Dimensional Deformable Granular Media. *Physical Review Applied*, *9*(2), 024028.
22. de Gennes, P. G. (1999). Granular matter: a tentative view. *Reviews of modern physics*, *71*(2), S374.
23. de Prunele, A., Ruffine, L., Riboulot, V., Peters, C. A., Croguennec, C., Guyader, V., ... & Germain, Y. (2017). Focused hydrocarbon-migration in shallow sediments of a pockmark cluster in the Niger Delta (Off Nigeria). *Geochemistry, Geophysics, Geosystems*, *18*(1), 93-112.
24. Di Felice, R., & Scapinello, C. (2010). On the interaction between a fixed bed of solid

material and the confining column wall: the Janssen approach. *Granular Matter*, *12*(1), 49-55.

25. Dupre, S., Scalabrin, C., Grall, C., Augustin, J. M., Henry, P., Şengör, A. M., Gorur, N., Cagatay, M., & Géli, L. (2015). Tectonic and sedimentary controls on widespread gas emissions in the Sea of Marmara: Results from systematic, shipborne multibeam echo sounder water column imaging. *Journal of Geophysical Research: Solid Earth*, *120*(5), 2891-2912.
26. Eriksen, J. A., Marks, B., Sandnes, B., & Toussaint, R. (2015). Bubbles breaking the wall: Two-dimensional stress and stability analysis. *Physical Review E*, *91*(5), 052204.
27. Fainerman, V. B., Makievski, A. V., & Miller, R. (2004). Accurate analysis of the bubble formation process in maximum bubble pressure tensiometry. *Review of scientific instruments*, *75*(1), 213-221.
28. Fauria, K. E., & Rempel, A. W. (2011). Gas invasion into water-saturated, unconsolidated porous media: Implications for gas hydrate reservoirs. *Earth and Planetary Science Letters*, *312*(1), 188-193.
29. Gill, D. & Lehane, B. (2001). An Optical Technique for Investigating Soil Displacement Patterns. *Geotechnical Testing Journal*, 24 (3), 324-329.
30. Holtzman, R., Szulczewski, M. L., & Juanes, R. (2012). Capillary fracturing in granular media. *Physical Review Letters*, *108*(26), 264504.
31. Huang, H., Zhang, F., Callahan, P., & Ayoub, J. A. (2012). Fluid injection experiments in 2D porous media. *SPE Journal*, *17*(03), 903-911.
32. Iskander, M. (2010). *Modelling with Transparent Soils: Visualizing soil structure interaction and multi phase flow, non-intrusively*. Springer Science & Business Media.
33. Hamilton, E. L. (1976). Variations of density and porosity with depth in deep-sea sediments. *Journal of Sedimentary Research*, *46*(2), 280-300.
34. Jang, J. (2014). *Gas-charged Sediments: Phenomena and Characterization* (Doctoral dissertation, Georgia Institute of Technology).
35. Jeng, D. S. (2003). Wave-induced sea floor dynamics. *Applied Mechanics Reviews*, *56*(4), 407-429.
36. Johnson, B. D., Boudreau, B. P., Gardiner, B. S., & Maass, R. (2002). Mechanical response of sediments to bubble growth. *Marine Geology*, *187*(3), 347-363.
37. Keulen, B. (2001). *Maximum Allowable Pressures during Horizontal Directional Drillings Focused on Sand* (Doctoral dissertation, TU Delft, Delft University of

Technology).

38. Krummel, A. T., Datta, S. S., Münster, S., & Weitz, D. A. (2013). Visualizing multiphase flow and trapped fluid configurations in a model three-dimensional porous medium. *AIChE Journal*, *59*(3), 1022-1029.
39. Lee, J. S., & Santamarina, J. C. (2005). Bender elements: performance and signal interpretation. *Journal of Geotechnical and Geoenvironmental Engineering*, *131*(9), 1063-1070.
40. Lewicki, J. L., Birkholzer, J., & Tsang, C. F. (2007). Natural and industrial analogues for leakage of CO2 from storage reservoirs: identification of features, events, and processes and lessons learned. *Environmental Geology*, *52*(3), 457-467.
41. Liu, J., & Iskander, M. G. (2010). Modelling capacity of transparent soil. *Canadian Geotechnical Journal*, *47*(4), 451-460.
42. Marchi, M., Gottardi, G., & Soga, K. (2013). Fracturing pressure in clay. *Journal of Geotechnical and Geoenvironmental Engineering*, *140*(2), 04013008.
43. Mayne, P. W. (2001). Stress-strain-strength-flow parameters from enhanced in-situ tests. In *Proc. Int. Conf. on In Situ Measurement of Soil Properties and Case Histories, Bali*.
44. Mayne, P. W., & Kulhawy, F. H. (1982). K_0- OCR Relationships in Soil. *Journal of the Soil Mechanics and Foundations Division*, *108*(6), 851-872.
45. Moridis, G. J., Collett, T. S., Pooladi-Darvish, M., Hancock, S., Santamarina, C., Boswel, R., Kneafsey, T., Rutqvist, J., Kowalsky, M., Reagan, M. T., Sloan, E. D., & Koh, C. (2011). Challenges, uncertainties, and issues facing gas production from gas-hydrate deposits. *SPE Reservoir Evaluation and Engineering*, *14*(1), 76-112.
46. Nedderman, R. M. (2005). *Statics and kinematics of granular materials*. Cambridge University Press.
47. Oppenheimer, J., Rust, A. C., Cashman, K. V., & Sandnes, B. (2015). Gas migration regimes and outgassing in particle-rich suspensions. *Frontiers in Physics*, *3*, 60.
48. Pietruszczak, S., & Pande, G. N. (1996). Constitutive relations for partially saturated soils containing gas inclusions. *Journal of Geotechnical Engineering*, *122*(1), 50-59.
49. Riboulot, V., Sultan, N., Imbert, P., & Ker, S. (2016). Initiation of gas-hydrate pockmark in deep-water Nigeria: Geo-mechanical analysis and modelling. *Earth and Planetary Science Letters*, *434*, 252-26
50. Saintyves, B., Dauchot, O., & Bouchaud, E. (2013). Bulk elastic fingering instability in hele-shaw cells. *Physical Review Letters*, *111*(4), 047801.

51. Sandnes, B., Flekkøy, E. G., Knudsen, H. A., Måløy, K. J., & See, H. (2011). Patterns and flow in frictional fluid dynamics. *Nature Communications*, *2*, 288.
52. Santamarina, J. C. (2003). Soil behavior at the microscale: particle forces. *Geotechnical Special Publication*, 25-56.
53. Santamarina, J. C., Klein, A., & Fam, M. A. (2001). *Soils and Waves*. J. Wiley and Sons, Chichester, UK.
54. Santamarina, J. C., Klein, K. A., Wang, Y. H., & Prencke, E. (2002). Specific surface: determination and relevance. *Canadian Geotechnical Journal*, *39*(1), 233-241.
55. Sauter, E. J., Muyakshin, S. I., Charlou, J. L., Schlüter, M., Boetius, A., Jerosch, K., Damm, E., Foucher, J., & Klages, M. (2006). Methane discharge from a deep-sea submarine mud volcano into the upper water column by gas hydrate-coated methane bubbles. *Earth and Planetary Science Letters*, *243*(3), 354-365.
56. Scandella, B. P., Varadharajan, C., Hemond, H. F., Ruppel, C., & Juanes, R. (2011). A conduit dilation model of methane venting from lake sediments. *Geophysical Research Letters*, *38*(6).
57. Scandella, B. P., Delwiche, K., Hemond, H. F., & Juanes, R. (2017). Persistence of bubble outlets in soft, methane-generating sediments. *Journal of Geophysical Research: Biogeosciences*, *122*(6), 1298-1320.
58. Schofield, A., & Wroth, P. (1968). *Critical State Soil Mechanics*. London: McGraw-Hill.
59. Shin, H., & Santamarina, J. C. (2010). Fluid-driven fractures in uncemented sediments: Underlying particle-level processes. *Earth and Planetary Science Letters*, *299*(1), 180-189.
60. Shin, H., & Santamarina, J. C. (2011a). Desiccation cracks in saturated fine-grained soils: particle-level phenomena and effective-stress analysis. *Geotechnique*, *61*(11), 961.
61. Shin, H., & Santamarina, J. C. (2011b). Open-mode discontinuities in soils. *Geotechnique Letters*, *1*(4), 95-99.
62. Shin, H., Santamarina, J. C., & Cartwright, J. A. (2008). Contraction-driven shear failure in compacting uncemented sediments. *Geology*, *36*(12), 931-934.
63. Sills, G. C., & Wheeler, S. J. (1992). The significance of gas for offshore operations. *Continental Shelf Research*, *12*(10), 1239-1250.
64. Skarke, A., Ruppel, C., Kodis, M., Brothers, D., & Lobecker, E. (2014). Widespread methane leakage from the sea floor on the northern US Atlantic margin. *Nature Geoscience*, *7*(9), 657-661.

65. Sperl, M. (2006). Experiments on corn pressure in silo cells–translation and comment of Janssen's paper from 1895. *Granular Matter*, *8*(2), 59-65.
66. Suckale, J., Keller, T., Cashman, K. V., & Persson, P. O. (2016). Flow-to-fracture transition in a volcanic mush plug may govern normal eruptions at Stromboli. *Geophysical Research Letters*, *43*(23).
67. Tary, J. B., Geli, L., Guennou, C., Henry, P., Sultan, N., Çağatay, N., & Vidal, V. (2012). Microevents produced by gas migration and expulsion at the seabed: a study based on sea bottom recordings from the Sea of Marmara. *Geophysical Journal International*, *190*(2), 993-1007.
68. Vanel, L., Claudin, P., Bouchaud, J. P., Cates, M. E., Clément, E., & Wittmer, J. P. (2000). Stresses in silos: comparison between theoretical models and new experiments. *Physical review letters*, *84*(7), 1439.
69. Varas, G., Ramos, G., Géminard, J. C., & Vidal, V. (2015). Flow and fracture in water-saturated, unconstrained granular beds. *Frontiers in Physics*, *3*, 44.
70. Wang, B., Socolofsky, S. A., Breier, J. A., & Seewald, J. S. (2016). Observations of bubbles in natural seep flares at MC 118 and GC 600 using in situ quantitative imaging. *Journal of Geophysical Research: Oceans*,*121*(4), 2203-2230.
71. Westbrook, G. K., Thatcher, K. E., Rohling, E. J., Piotrowski, A. M., Pälike, H., Osborne, A. H., ... & Hühnerbach, V. (2009). Escape of methane gas from the seabed along the West Spitsbergen continental margin. *Geophysical Research Letters*, *36*(15).
72. Wheeler, S. J. (1988). A conceptual model for soils containing large gas bubbles. *Geotechnique*, *38*(3), 389-397.
73. Wheeler, S. J. (1990). Movement of large gas bubbles in unsaturated fine-grained sediments. *Marine Georesources & Geotechnology*, *9*(2), 113-129.
74. Wood, D. M. (1990). *Soil Behaviour and Critical State Soil Mechanics*. Cambridge university press.
75. Yu, H. S. (2013). *Cavity Expansion Methods in Geomechanics*. Springer Science & Business Media.
76. Yu, H. S., & Rowe, R. K. (1999). Plasticity solutions for soil behaviour around contracting cavities and tunnels. *International Journal for Numerical and Analytical Methods in Geomechanics*, *23*(12), 1245-1279.
77. Zhang, F., Damjanac, B., & Huang, H. (2013). Coupled discrete element modeling of fluid injection into dense granular media. *Journal of Geophysical Research: Solid*

Earth, *118*(6), 2703-2722.

Table 1. Transparent soil: geotechnical properties.

Property	Value	Note
Particle size/ Aggregate size	~30 nm/ ~1 μm	From SEM image of fumed silica powder
Specific surface S_s	200 m^2/g	Methylene blue method(4)
Liquid Limit *LL*	393%	From fall cone test
Hydraulic conductivity *k*	2.2×10^{-7} cm/s	At σ'=44 kPa, from consolidation tests
Coefficient of consolidation c_v	~1.3 × 10^{-3} cm^2/s	From consolidation tests
Compression index C_c (1)	~3.3	
Void ratio e_{1kPa}	23.3	
Small-strain shear stiffness	0.3 MPa	At σ'=44 kPa , from shear wave velocity
Velocity-stress(2) α factor(1)	3.34 m/s	From shear wave velocity
Velocity-stress β factor(1)	0.543	
Friction angle ϕ	30°(3)	Angle of repose
Coefficient of friction μ	0.4	Shear against Plexiglas substrate

Note: (1) Properties are determined using an oedometer cell instrumented with bender elements for concurrent shear wave velocity measurements [Lee and Santamarina, 2005]. Measured parameters are consistent with fine-grained soils [Cha et al., 2014].

(2) $V_s = \alpha \left(\frac{\sigma'_o}{1kPa} \right)^{\beta}$

(3) Gill and Lehane (2001) measured ϕ=31° in triaxial tests.

(4) Santamarina et al., 2002

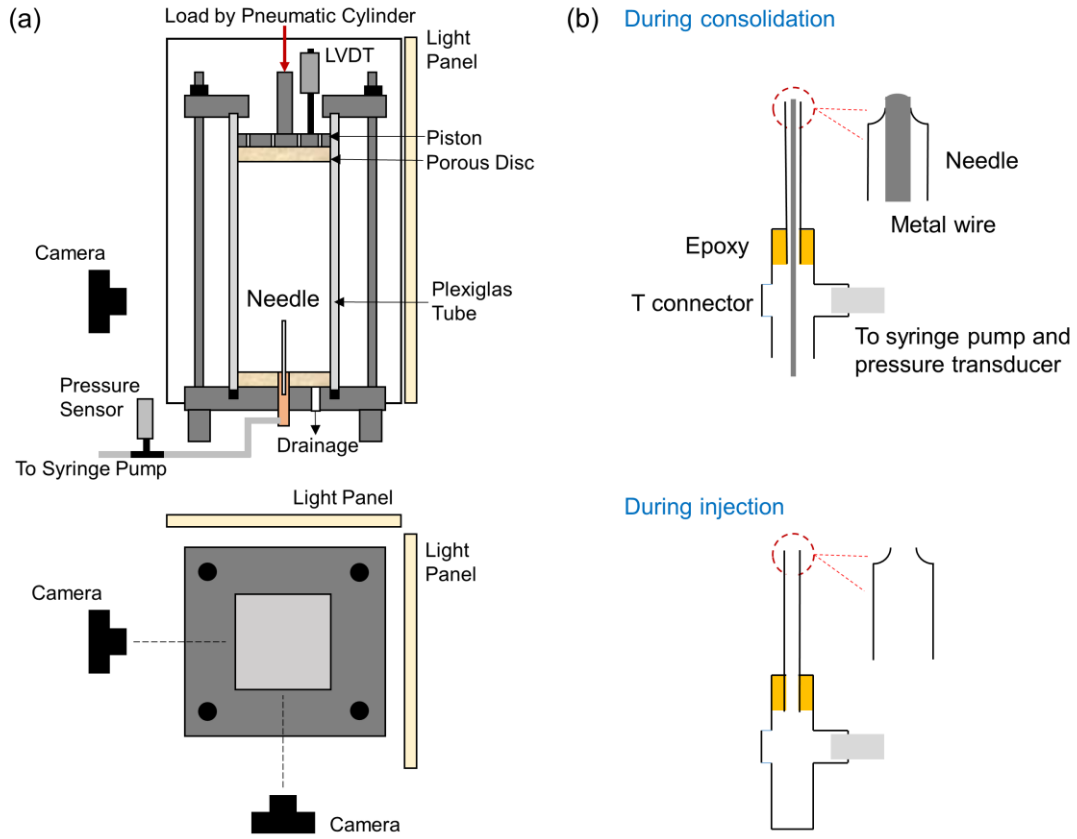

Figure 1. Experimental setup. (a) Frame, cell, and monitoring system - side view and cross section. (b) Details of the gas injection needle.

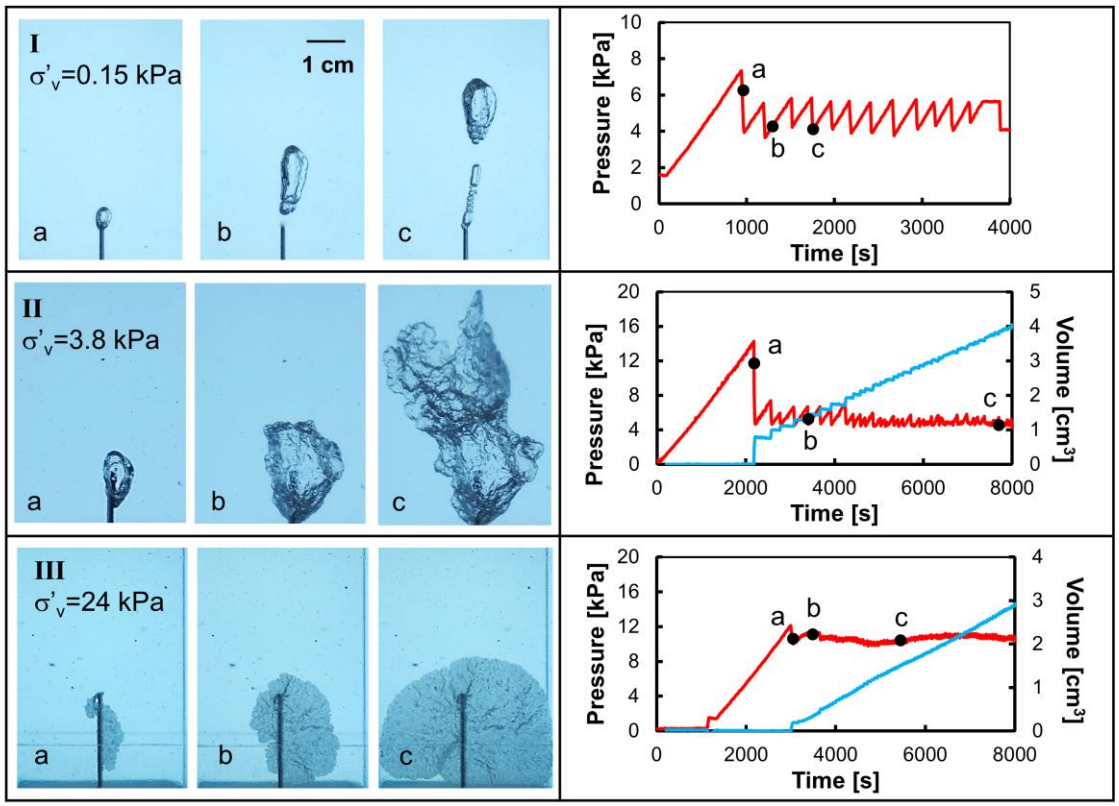

Figure 2. Typical displacive gas migration patterns. Plots on the right show gas pressure (red line) and gas inclusion volume (blue line) signatures.

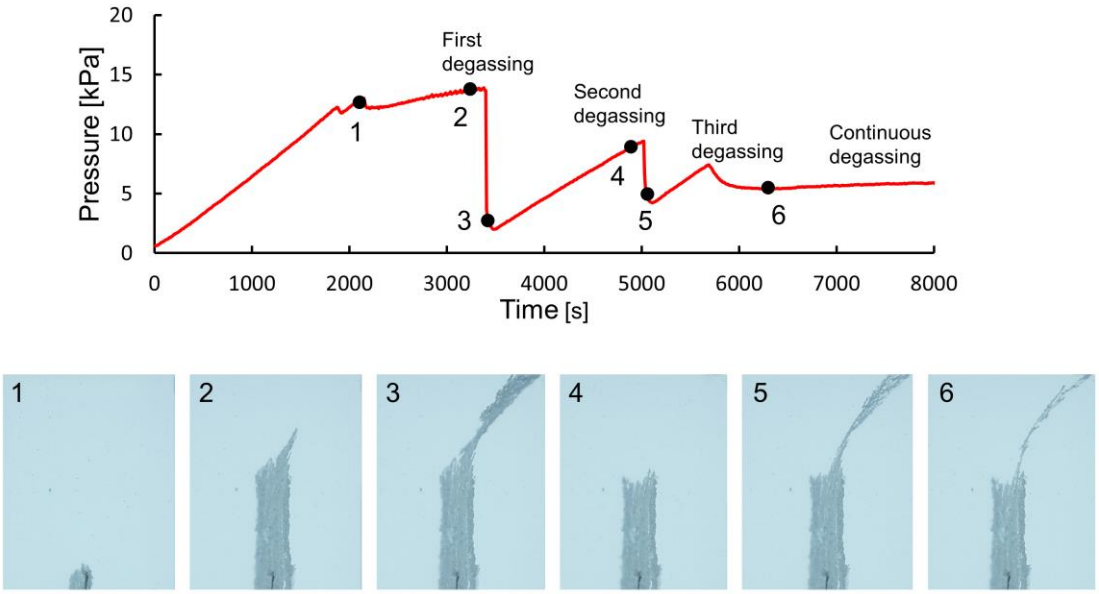

Figure 3. Stress history and sequential injection-degassing events. The specimen was pre-consolidated to 44 kPa and then unloaded to 1.4 kPa before gas injection. There is principal stress rotation in the upper part where the upwards propagating fracture changes direction. The sediment "heals" after the first degassing event, but leaks continuously after the third event. Successive gas leak pathways follow the same trajectory.

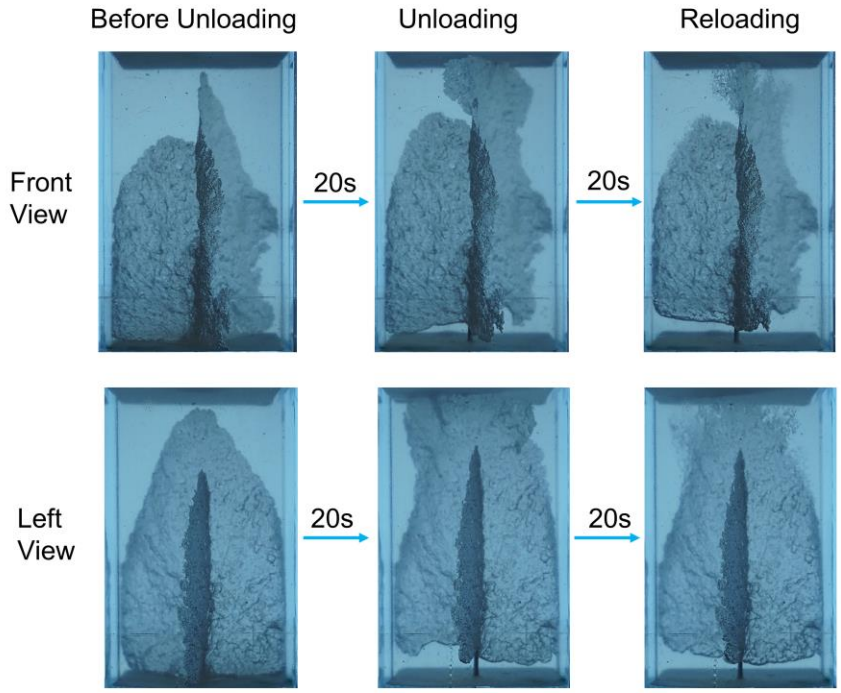

Figure 4. Pressure fluctuations promote the upwards migration of gas-filled openings. Y-shaped gas fracture (Note: unloading from 14 kPa).

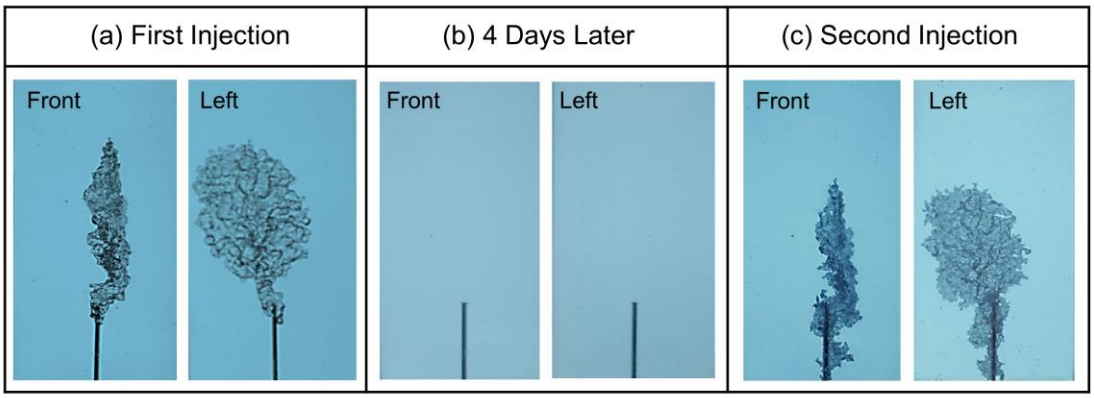

Figure 5. Memory effect. (a) Open-mode gas-filled fracture after the first injection. (b) Gas diffusion and fracture healing 4 days after the first injection. (c) Gas-filled fracture after the second injection.

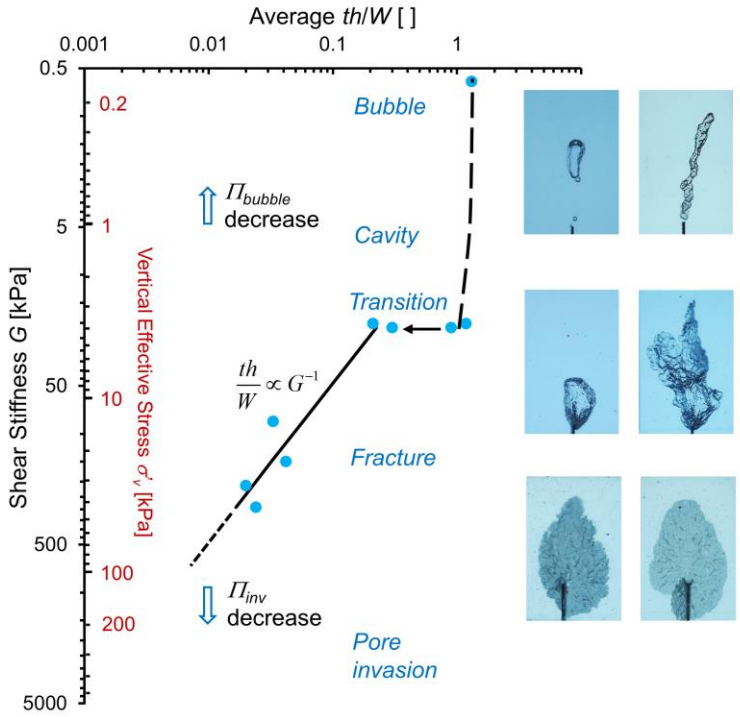

Figure 6. Gas migration patterns in sediments as a function of effective stress and sediment stiffness. The average fracture thickness-to-width ratio *th*/*W* is a linear function of sediment compliance G^{-1}.

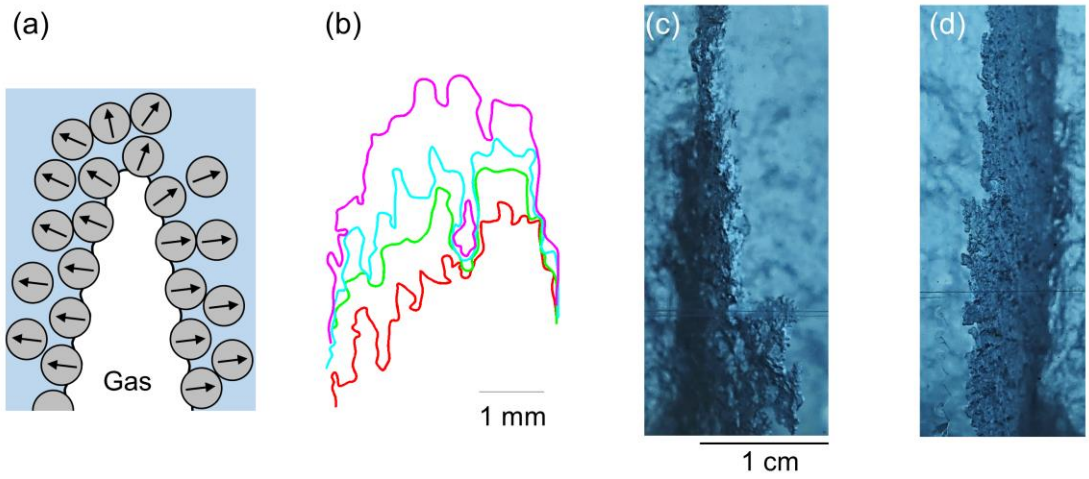

Figure 7. Grain-displacive gas migration. (a) Grain-scale forces. (b) Instantaneous fracture fronts at different stages of injection (front view). (c & d) Irregular and discontinuous fracture front (side views).

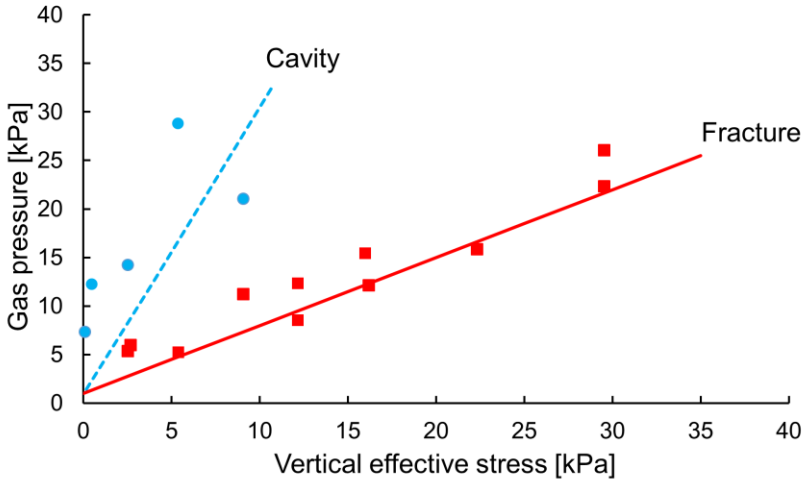

Figure 8. Gas injection pressure vs. vertical effective stress for cavity expansion and open-mode fractures. Data: red squares identify observed fractures; blue circles correspond to cavity expansion (peak pressure). Models: the solid red line is for fracture propagation (Equation 4, k_0=0.7), and the dashed blue line shows the cavity expansion pressure (Equation 2).